Helium Ion Microscope Fabrication Causing Changes in the Structure and Mechanical Behavior of Silicon Micropillars

Yue-Cun Wang, Lin Tian, Fan Liu, Yuan-Bin Qin, Gong Zheng, Jing-Tao Wang, Evan Ma, and Zhi-Wei Shan**

The ability to machine and polish materials controllably on the micro- and nanoscale, and to observe the morphological evolution of the products being fabricated, is essential for today's advances in nanotechnology. Recently, state-of-the-art helium ion microscope (HIM) has become a popular tool in this regard.[1–4] HIM has several advantages, when compared with the widely used gallium ion microscope (often cited as focused ion beam, FIB) for the fabrication and examination of micropillars. First of all, HIM offers a better spatial resolution and more precise micromachining capability. Second, being an inert gas, helium does not interact chemically[5] with the material, and therefore is expected to produce cleaner samples than those fabricated by Ga^+-based FIB. However, He^+ is much lighter than Ga^+ (Ga^+ 69.723 amu, He^+ 4.003 amu) with the similar Pauling ionic radii (Ga^+ 81 pm, He^+ 93 pm).[6] As a consequence, helium ions have a lower energy loss rate during implantation[7] and can reach further inside the sample volume, by more than one order of magnitude in depth, than the thin surface layer expected for gallium ions. For example, at the typical beam energy of 30 keV, He^+ can penetrate several hundreds of nanometers,[8] while it is only 25–30 nm[9,10] for Ga^+. The projected range of He^+ can be comparable to the dimensions of the micropillars, extending radiation damage well into the sample interior, and therefore can affect the structure and properties of a rather large portion of the material.[8] This is compounded by the high dose of He^+ ions required for nanofabrication, typically on the order of 10^{17}–10^{18} ions cm^{-2}, due to the low sputtering yield of light helium ions.[1] The potential radiation effect is thus an important aspect that needs to be kept in mind, for the proper use of HIM, as well as for the interpretation of the properties observed in the resultant samples. This issue unfortunately has not received much attention and remains to be carefully studied.

In this work, the effects of He^+ on the structure and mechanical behavior of Si micropillars have been quantitatively and systematically evaluated inside a transmission electron microscope (TEM), in a He^+ dosage range typically used for nanofabrication. Si is chosen here as a model case because it is the most widely used semiconductor material, and also a popular choice for micro-electromechanical system (MEMS) and nano-electromechanical system (NEMS) components such as batch-fabricated sensors and transducers.[11] In addition, the behavior of Si upon He^+ irradiation, all by itself, has been of interest to the semiconductor industry and extensively applied.[8,12–23]

Considering the low sputtering yield of light He^+, to quickly produce micropillars we first used the highly efficient FIB milling (Field Electron and Ion Company (FEI) Helios NanoLab 600, 30 keV Ga^+, beam current ranging from 9.7 to 0.28 nA) for the heavy-duty material removal directly from the boron-doped ⟨001⟩-oriented single crystalline Si wedge. This Si wedge was initially designed to facilitate the compression tests on particles inside TEM and more details about the geometry of the Si wedge can be found in ref. [24]. The semifinished Si pillars have diameters about 300 nm, and the aspect ratio (height to diameter) of ≈2. The rough blanks fabricated by Ga^+ were then placed in a HIM (Carl Zeiss Orion NanoFab), for further polishing using a subnanometer sized He^+ probe at a current of 7–8 pA with a landing energy of 28.4 keV. The Si pillars were polished with grazing beam incidence on the sidewall and the roughly estimated glancing angle β was ≈2° (β = 90° would correspond to normal incidence into the pillar side surface), and He^+ milling process was illustrated in Figure S1 (Supporting Information). For the HIM system we used, redeposition phenomena will become quite obvious if

Y.-C. Wang, Dr. L. Tian, Dr. Y.-B. Qin, Prof. E. Ma, Prof. Z.-W. Shan
Center for Advancing Materials Performance from the Nanoscale
State Key Laboratory for Mechanical Behavior of Materials
Xi'an Jiaotong University
Xi'an 710049, P. R. China
E-mail: ema@jhu.edu; zwshan@mail.xjtu.edu.cn

F. Liu, Prof. J.-T. Wang
School of Materials Science and Engineering
Nanjing University of Science and Technology
Nanjing 210094, P. R. China

G. Zheng
Engineering Research Center of Materials Behavior and Design
Ministry of Education
Nanjing University of Science and Technology
Nanjing 210094, P. R. China

Prof. E. Ma
Department of Materials Science and Engineering
Johns Hopkins University
Baltimore, MD 21218, USA

DOI: 10.1002/smll.201601753

© 2016 Wiley-VCH Verlag GmbH & Co. KGaA, Weinheim

the fabrication rate is high. On the other hand, if the milling time is too long, the time-dependent thermal drift will affect the geometry of fabricated samples. Consequently, in order to get samples with exactly designed geometry and without obvious redeposition, we have to optimize the machining rate by adjusting the He^+ ions dosage or ion beam current. The exposure time to helium beam during imaging was minimized as short as possible for avoiding additional He^+ implantation.

Figure 1a schematically illustrates the two-step microfabrication process. Comparing the inset representative scanning electron microscope (SEM) images of the FIBed (Figure 1b) and He^+-polished (Figure 1c) Si pillars, we see that the former pillar has a large taper angle $\alpha = \approx 7°$ and the fine He^+ polishing makes the nearly perfect geometry ($\alpha < 2°$). The resolution of FIB is limited by the Ga^+ energy spread generated from the liquid metal ion source, and its sputter yield is also too large for accurate patterning control over very short lateral distances. In comparison, the gaseous field ionization source of HIM does not suffer from the energy spread and subsequent chromatic aberration, and its probe size can be as small as 0.4 nm.[25] The uniform exteriors of the two samples in SEM images, except for the taper, do not display any other differences. The chemical compositions of samples were analyzed using energy-dispersive X-ray spectroscopy (EDX). The EDX analysis shown in Figure 1b,c reveals that the undesirable gallium and carbon introduced during FIB fabrication have been removed by He^+ polishing. The presence of slight oxygen in both samples should be caused by exposure to air. Because of the intrinsic limitation of EDX, no helium signal has been detected.

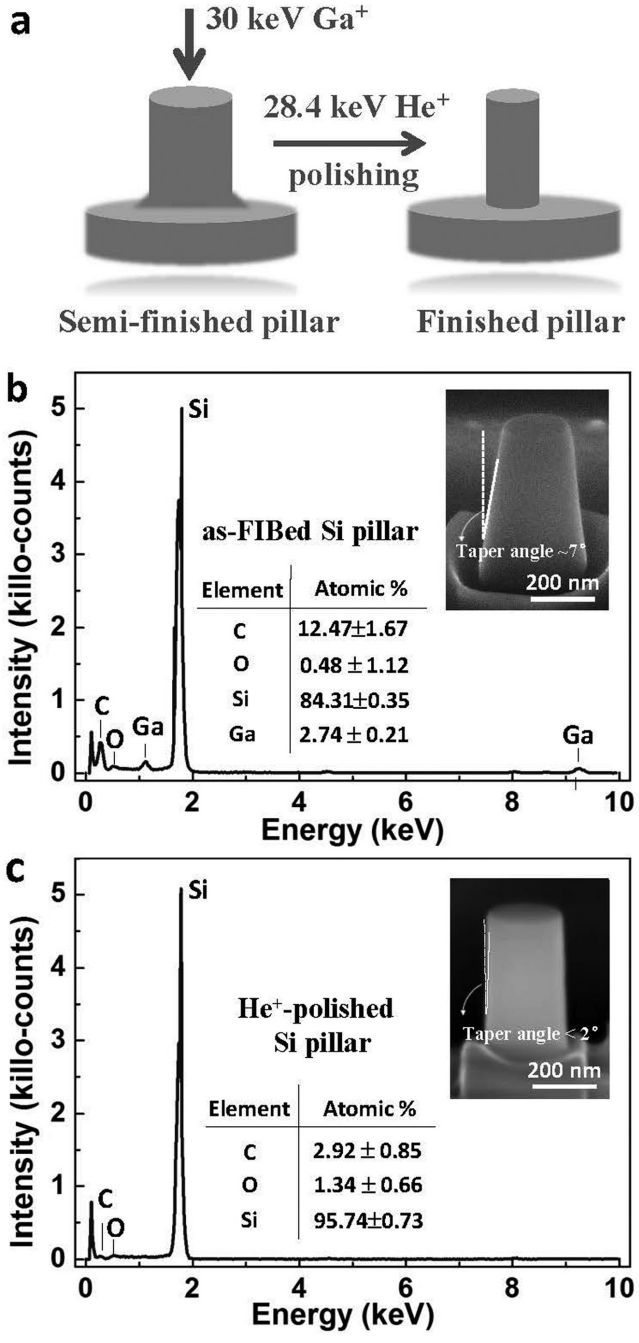

Figure 1. Characterization of the as-FIBed and He^+-polished Si pillars. a) Schematic representation of the two-step fabrication process. b,c) EDX spectra of a typical as-FIBed Si pillar b) and a He^+-polished Si pillar c). The inset SEM images show their different exterior appearance.

The distributions of implanted ions and displaced Si atoms were simulated using the SRIM (the stopping and range of ions in matter)[26] software based on the Monte Carlo simulation (Figure S2, Supporting Information). Helium ions penetrate about ten times deeper than gallium ions due to their lower energy loss rate, and they remain relatively collimated within about one hundred nanometers. The preponderance of the dislocated Si atoms in the case of gallium ions illustrates that Ga^+ radiation produces more significant and localized damage. The helium ions lose energy primarily by electron interaction instead of nucleus collision, so they produce much lower density of lattice damage (atomic collision cascades) than the Ga^+.[7]

TEM observation found that there was an obvious amorphous layer on the as-FIBed crystalline Si (c-Si) pillar, and one typical example with a ≈28 nm amorphous Si (a-Si) shell is shown in **Figure 2**a. The high resolution TEM (HRTEM) image of the a-Si/c-Si interface also proves the existence of a-Si. The inset selected area electron diffraction pattern (SADP) illustrates that the vast majority of the pillar volume remains single crystalline. Statistical measurements showed that the thickness of the a-Si shell was always 25–30 nm, regardless of the diameter of the pillars when 30 keV Ga^+ was used.[10] This agrees well with the Monte Carlo simulation result that Ga^+ produces significant but only localized damage very close to the surface. The situation is very different for the He^+ beam irradiation: the structure of the pillar interior is now subject to major changes. It was reported that Si could also be amorphized by He^+ bombardment, when the dosage is sufficiently high ($>10^{17}$ ions cm^{-2}).[7,27] Considering the much larger penetrating depth of helium ions (Figure S2, Supporting Information), we expected the entire Si micropillar to turn amorphous after He^+ polishing directly from the semifinished c-Si blanks. The surface layer with thickness of ≈50 nm was milled away and simultaneously, the helium ions were implanted deep into Si during polishing. Figure 2b–d shows some typical pillars irradiated to a He^+ dose of 2.0×10^{17}, 5.4×10^{17}, and 1.6×10^{18} ions cm^{-2}, respectively. These Si pillars had similar

© 2016 Wiley-VCH Verlag GmbH & Co. KGaA, Weinheim

DOI: 10.1002/smll.201601753

small NANO MICRO

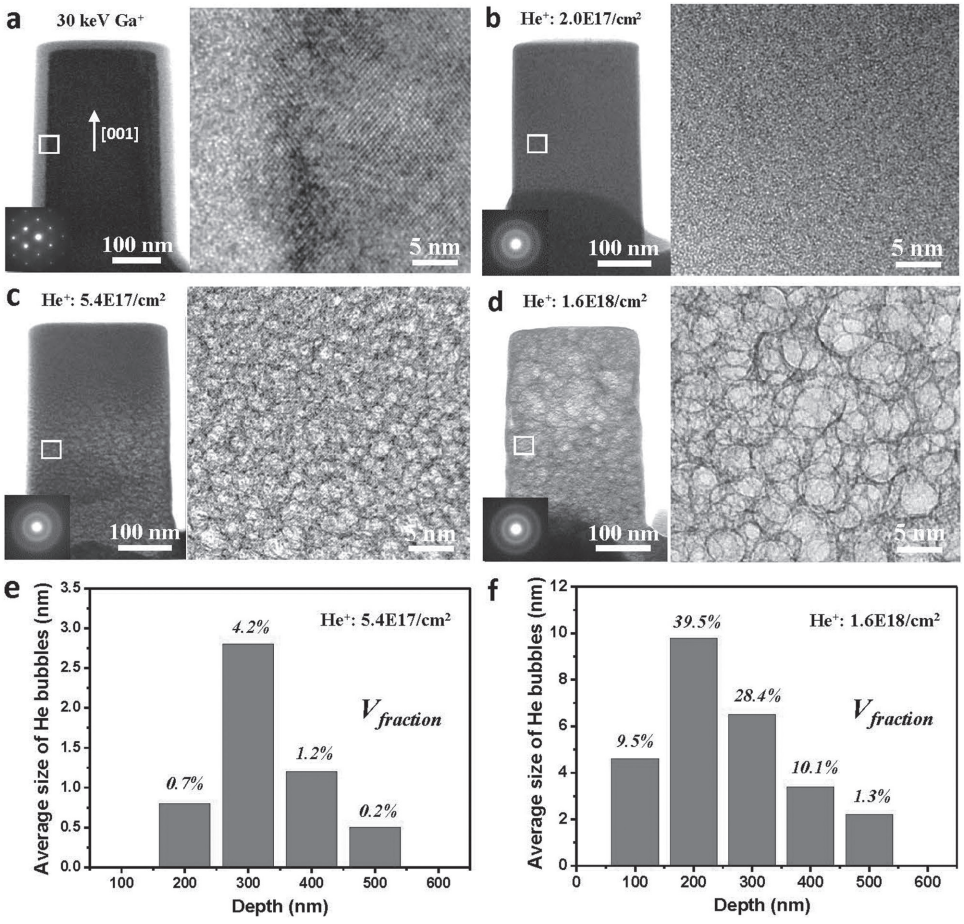

Figure 2. TEM characterization of the Ga^+-FIBed and He^+-implanted Si pillars. a) Bright-field TEM image (left) of the as-FIBed c-Si pillar with a Ga^+ bombardment-induced a-Si surface layer and the HRTEM image (right) of the framed a-Si/c-Si interface zone. The inset SADP shows the orientation of the single crystalline pillar. b) Complete amorphization of Si pillar after the 2.0×10^{17} ions cm^{-2} He^+ polishing. The inset SADP and HRTEM image (right) confirm the amorphous microstructure. c) At the dosage of 5.4×10^{17} ions cm^{-2}, small helium nanobubbles formed in the interior of the a-Si pillar. d) With further increasing dosage to 1.6×10^{18} ions cm^{-2}, the nanobubbles are found all over a-Si pillar, and some big bubbles with a maximum size of ≈20 nm concentrate in middle section of the pillar. The average size distribution of the helium nanobubbles along the longitudinal depth direction in the He^+-implanted Si pillars with the dosage of 5.4×10^{17} ions cm^{-2} e) and 1.6×10^{18} ions cm^{-2} f). e) and (f) also show the estimated volume fraction of helium nanobubbles ($V_{fraction}$) in different zones of the Si pillars.

diameters, $d = 250 \pm 20$ nm. At the dose of 2.0×10^{17} ions cm^{-2} (Figure 2b), the pillar was indeed amorphized completely, as evidenced from the uniform contrast in bright-field TEM image, the diffuse ring in SADP and the HRTEM image of the framed zone. Though the bombardment from light He^+ produces fewer dislocated Si atoms compared with Ga^+, the implanted helium can reach further and effectively trap the irradiation-induced point defects, for example the vacancies. This interaction of helium atoms with defects prevents them from recombination with the interstitial defects, and the following defects accumulation can favor the amorphization of Si.[5] When the He^+ dose was increased to 5.4×10^{17} ions cm^{-2}, nanobubbles with 1–3 nm sizes appeared in the middle section of the amorphous Si pillar (HRTEM image in Figure 2c). The helium bubbles could be clearly seen in the under-focused TEM image with the defocus value of 800–1000 nm. A further threefold increase in dose to 1.6×10^{18} ions cm^{-2} made the whole Si pillar porous and the diameter range of helium bubbles increased to 1–20 nm (HRTEM image in Figure 2d). The large helium bubbles (>10 nm) were mainly formed in the middle part of the pillar, which remained amorphous as the bubbles expanded in size (see the inset diffuse rings in Figure 2c,d). Due to the low mobility and solubility of helium in a-Si,[19,28] the implanted helium ions are all trapped subsurface and deformed the a-Si to form balloon-like big bubbles firstly in the region with high enough He^+ dosage.

The size distributions of the helium nanobubbles and their volume fraction ($V_{fraction}$) in the He^+-implanted Si pillars with the dosage of 5.4×10^{17} ions cm^{-2} (see Figure 2e) and 1.6×10^{18} ions cm^{-2} (see Figure 2f) have been characterized. Some small zones (near the side wall of Si pillars) with the area $s = 40$ nm $\times$ 40 nm were selected first and then magnified for counting bubbles' numbers N in them and measuring the diameter of each bubble. By assuming the helium nanobubbles to be spherical, the average size of the bubbles in each zone can be calculated. Their volume fraction can be roughly estimated according to the following equation

DOI: 10.1002/smll.201601753
© 2016 Wiley-VCH Verlag GmbH & Co. KGaA, Weinheim

$$V_{\text{fraction}} = \frac{V_{\text{bubbles}}}{s \times t} \quad (1)$$

where V_{bubbles} is the total volume of helium bubbles and can be estimated according to the numbers and sizes of spherical bubbles; t is the thickness of selected zones (roughly regarded as 100 nm). The bubbles average size distributions along the longitudinal depth direction of pillars were plotted in the bar graphs, in which the corresponding V_{fraction} was marked. The bubbles size distributions in both pillars implanted with different He^+ dosages are consistent with the V_{fraction} trend.

We next examine one typical case of the pure a-Si pillar polished by He^+ (He^+ dose is 4×10^{17} ions cm^{-2} with the beam energy of 28.4 keV). Because the helium concentration and radiation damage extent in the pillar is relative low, no detectable helium bubbles can be observed directly from the TEM image. The helium concentration (He-at%) and radiation damage (primary knock-on atoms based on the Kinchin–Pease model[29]) distributions across one typical pillar were simulated using the SRIM software. The chemical effect from helium implantation is not considered due to the extremely low reactivity of inert gas with other substances. The resultant He-at% and radiation damage measured in dpa (displacements per atom) within the a-Si pillar were non-uniform with more helium and damage in the middle range (Figure S3, Supporting Information). Both the He-at% and displacements per atom are proportional to the He^+ dose, so at the constant beam energy their distributions (except for the peak values) along the penetration depth would keep unchanged with the increasing He^+ dosage.[7,29] The helium nanobubbles' size distributions along the longitudinal direction of pillars (Figure 2e,f) indicated that the helium ions were mainly trapped in the middle part of the pillar, and this is roughly consistent with the He-at% and radiation damage distributions simulated through SRIM (Figure S3, Supporting Information).

We now turn our attention to the mechanical properties of these Si pillars as a function of He^+ ion dosage. Several in situ quantitative compression tests were performed on these He^+-bombarded a-Si pillars with different doses inside TEM. Their representative engineering stress–strain curves in orange, green, and red are shown in **Figure 3**a. The yield stress at which the pillars started deviating from the elastic behavior decreases markedly as the He^+ dose increased. We also compressed a-Si pillars with no exposure to He^+ (i.e., 0 He^+ ions cm^{-2}) for comparison: they were micromachined using FIB (Ga^+) from the plasma-enhanced chemical vapor deposition (PECVD) a-Si film (see the Experimental Section). The FIBed a-Si pillar had the similar engineering stress–strain curve (blue) with that of the He^+ irradiation-induced pure a-Si pillars (orange). However, the morphologies of the two kinds of a-Si pillars after compression were quite different. For the Ga^+-fabricated a-Si pillar, the plastic strain was mainly concentrated on its top part and formed a mushroom-like geometry (Figure 3b). This can be expected, as the maximum implantation depth in Si for the glancing angle 30 keV Ga^+ beam is only several tens of nanometers.[26] It should be noted that in order to avoid the taper effect accompanied with cylindrical pillars, all the FIBed Si pillars

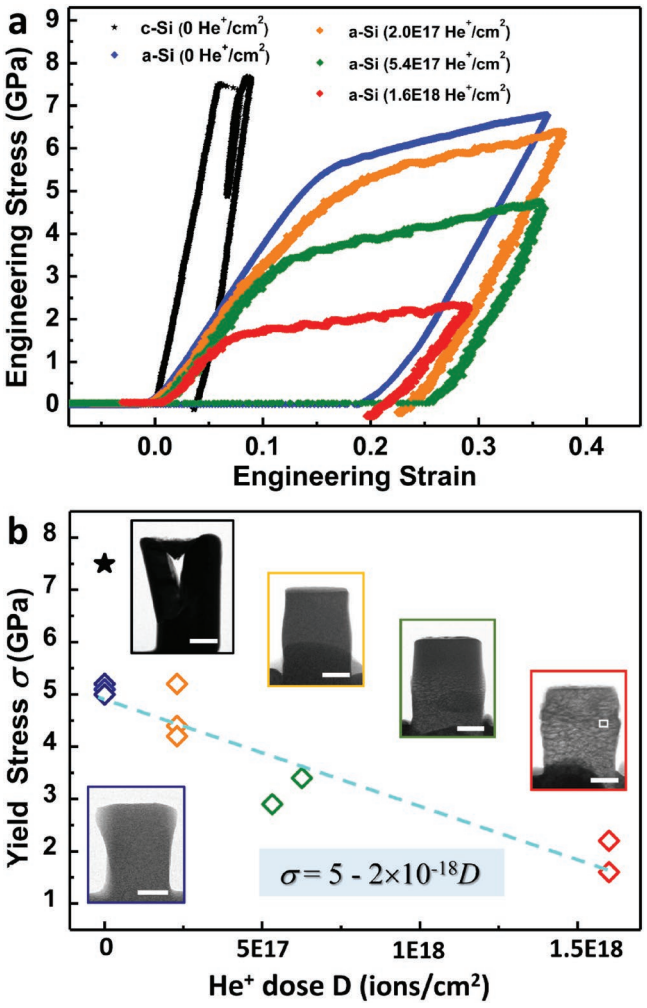

Figure 3. Mechanical behaviors of c-Si, FIBed a-Si, and He^+-implanted a-Si samples with different dosages under compression. a) Representative engineering stress–strain curves of the c-Si pillar (black, d = 234 nm), as-fabricated a-Si pillar (blue, d = 242 nm), He^+-implanted a-Si pillars with increasing doses (orange, d = 257 nm; green, d = 266 nm; red, d = 246 nm). b) Reduction in yield strength with increasing helium ions dose and the corresponding bright-field TEM images of the different Si pillars after compression. Note that the c-Si (black solid star spot) has high strength but cracks. The scale bars represent 100 nm.

used in this work have square-like cross-section, and more details can be found in Figure S4 (Supporting Information). In contrast, for the He^+-implanted a-Si pillars, the deformation mainly occurred in their middle region, resulting in a drum-like geometry (Figure 3b), in accordance with the SRIM calculated location (Figure S3, Supporting Information) of the maximum helium concentration and irradiation damage. As such, the most softened regions in the ion-implanted a-Si can be predicated based on the kinds of incident ions and their energy.

Unlike the stable plastic flow of ion-implanted a-Si pillars, the c-Si micropillars failed in brittle manner without obvious plastic deformation. As shown in Figure 3b (the inset), a splitting crack was generated during the sudden strain burst (the black stress–strain curve). Meanwhile, the brittle c-Si has a much higher strength of ≈7.5 GPa (marked by the black star in Figure 3b) than a-Si. More details about the c-Si

© 2016 Wiley-VCH Verlag GmbH & Co. KGaA, Weinheim

small 2016,
DOI: 10.1002/smll.201601753

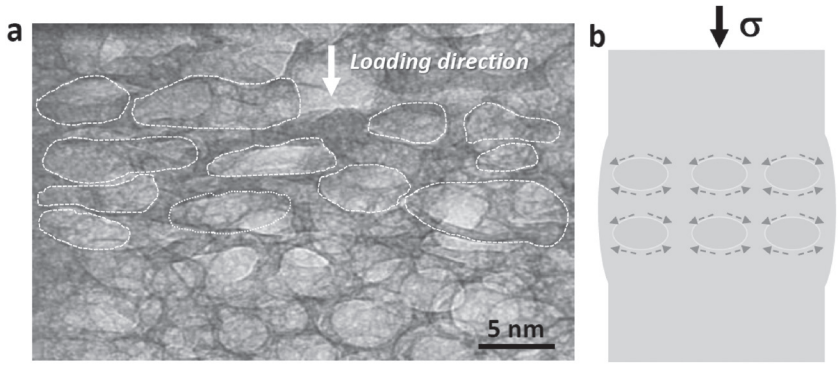

Figure 4. Helium nanobubbles' distribution in the deformed zone. a) HRTEM image of the flattened helium nanobubbles outlined by the white dashed curves. b) Illustration of the plastic flow (dashed arrows) of the Si atoms around bubbles.

micropillars can be found in ref. [10]. Our findings agree well with the indentation tests: ion implantation amorphized Si had a greater degree of plastic deformation and lower hardness compared with crystalline Si.[30]

The yield strength of the He^+-implanted a-Si micropillars decreased almost linearly with increasing He^+ dosage (fitted by the blue dotted line in Figure 3b), and this increasing softening with ion dosage can be attributed to the increasing extent of radiation damage. Defects such as broken (or weakened) bonds[31,32] can be caused by the bombardment of energetic ions, especially in the collision cascades. Larger ions dosage will create more defects and make the sample weaker. As a result of collisions, the degree of disorder in the sample will increase, as can be evidenced by the broadening of transverse optical peak in Raman spectrum.[33] Although the overall density of a-Si might not change,[34] the heterogeneity increase significantly with the generation of excess free volume[35] and the liquid-like regions.[36] Both of them act as plasticity carriers in a-Si. The former contributes to the homogeneous deformation of glassy materials while the latter has lower shear moduli. The combination of these two kinds of defects leads to a radiation-enhanced plastic flow with a relatively small shear viscosity and the dosage dependent softening.[37]

The morphology of helium nanobubbles after compression can be used to infer the deformation mode. We took the compressed Si pillar with high density nanobubbles (see its initial image in Figure 2d, 1.6E18 ions cm^{-2} dose) for example. The initial balloon-like helium nanobubbles were flattened to ellipsoid shape (outlined by the white dashed curves in **Figure 4**a) and they align approximately along the direction perpendicular to the loading stress vector. By comparing the HRTEM images in Figures 2d and 4a, we find that the volume of the bubbles had no obvious change in the balloon or ellipsoid shape, suggesting that the helium nanobubbles deform through a stress-driven plastic flow of their surrounding a-Si materials, rather than "pops" of themselves (see the illustration in Figure 4b). Presumably, homogeneous plastic deformation of the high density helium nanobubbles should make it difficult to activate and propagate highly localized shear bands, allowing more distributed flow of the He^+-implanted a-Si to come into play under compressive condition.

Based on our findings, it can be speculated if the He^+ beam acceleration voltage (in the range of 25–55 kV for nanofabrication, 28.4 kV in this work) is increased, the helium ions can penetrate much deeper and the pure a-Si micropillars with larger size may be obtained at the same dosage. The fact that the HIM-induced amorphous Si structure and the helium nanobubbles kept unchanged after exposure in air for two months suggested that they quite stable at the ambient temperature. What is more, the orientation of the single crystalline Si as starting material may make the final structure or the mechanical properties of the He^+-implanted samples different,[38] and this deserves further study in the future.

In summary, we have micromachined Si pillars using focused He^+ beam in a helium ion microscope. This resulted in pillars with no taper and free from gallium contamination. But over a range of He^+ dosages > $\approx 10^{17}$ ion cm^{-2}, which is typically experienced by samples in HIM nanofabrication, the c-Si pillars turned completely amorphous. Helium nanobubbles form and grow in the a-Si at the high end of the He^+ doses we used. That is, with the increasing He^+ dosage, the microstructure of Si pillars evolve gradually from dense amorphous state to amorphous-bubble composite. The resultant amorphous pillars are softened due to accumulated ion beam damage, exhibiting drastic strength reduction with increasing He^+ dose. Special attention should therefore be paid to the helium ion effects, when the Si samples are micromachined or imaged in the HIM. These findings are important, considering the wide application of Si in computer and MEMS devices, and the increasing use of FIB and HIM in these industries. The same can also be said in general, for all materials sensitive to radiation damage: caution should be exercised to guard against structure and property changes that may be incurred in the samples under the highly penetrative He^+ ion beam. On the optimistic side: firstly, the location of the softened zone can be well controlled, predictable by calculating the depth profile of radiation damage for the ion energies used, and the yield strength could also be manipulated by tuning the helium ion dose; secondly, the combination of microfabrication and He^+ implantation may provide an easy and noncontaminating way to study the effects of helium irradiation on the microstructure and mechanical behaviors of nuclear materials at submicrometer/nano scale. Finally, we note that the beam-altered properties can also have a beneficial effect: the irradiated a-Si, being more compliant and ductile, could be a useful structural material for certain MEMS/NEMS applications, and be amenable to reshaping via deformation under externally imposed stresses.

Experimental Section

Deposition of the a-Si Film by PECVD: Amorphous Si film was deposited on the above mentioned ⟨001⟩-oriented c-Si wedge substrate using a PECVD instrument with the radio frequency (RF)

DOI: 10.1002/smll.201601753
© 2016 Wiley-VCH Verlag GmbH & Co. KGaA, Weinheim

power of 20 W, at 250 °C substrate temperature, 800 mTorr process pressure, pure SiH_4 flow rate of 30 sccm, and Ar flow rate of 475 sccm. The deposited a-Si film adhered firmly to the substrate surface, and no obvious voids have been found during the FIB milling process. The as-FIBed a-Si pillars from the a-Si film have a uniform microstructure (see the bright-field TEM image in Figure 4b).

EDX: EDX (JED-2300T) was conducted in the JEOL 2100F TEM in the scanning transmission electron microscopy (STEM) mode for high resolution. Five points were randomly chosen from different regions on the FIBed and helium-implanted Si pillars, respectively.

Uniaxial Compression Tests in TEM: The samples were tested in a JEOL 2100F TEM at 200 kV with a Hysitron PI95 TEM PicoIndenter under a constant displacement rate control of 5 nm s^{-1}. The diameter of the flat diamond punch was ≈5 µm. The engineering stress was defined as the ratio of the measured load to the nominal cross-sectional area of the pillar, and the engineering strain was calculated to be the ratio of the deformation displacement of the pillar to its initial height. The yield point was determined by visually inspecting the curve for the first deviation from linear elastic loading and the yield stress was defined as the engineering stress at this yield point. All the pillars for compression have similar sizes, with $d = 250 \pm 20$ nm.

Supporting Information

Supporting Information is available from the Wiley Online Library or from the author.

Acknowledgements

Z.-W.S. and Y.-C.W. gratefully acknowledge the financial support from National Natural Science Foundation of China, NSFC (51231005 and 51321003). L.T. thanks NSFC (51501144) and China Postdoctoral Science Foundation (2015M580842). J.-T.W. would like to thank the NSFC No. 51520105001. The authors also gratefully thank Mingshuai Ding and DanLi Zhang at Xi'an Jiaotong University for the valuable discussions.

[1] A. I. Kuznetsov, A. E. Miroshnichenko, Y. H. Fu, V. Viswanathan, M. Rahmani, V. Valuckas, Z. Y. Pan, Y. Kivshar, D. S. Pickard, B. Luk'yanchuk, *Nat. Commun.* **2014**, *5*, 3104.
[2] M. Barr, A. Fahy, J. Martens, A. P. Jardine, D. J. Ward, J. Ellis, W. Allison, P. C. Dastoor, *Nat. Commun.* **2016**, *7*, 10189.
[3] D. Maas, E. van Veldhoven, P. Chen, V. Sidorkin, H. Salemink, E. van der Drift, P. Alkemade, *SPIE Adv. Lithogr.* **2010**, *14*, 7638.
[4] J. Morgan, J. Notte, R. Hill, B. Ward, *Microsc. Today* **2006**, *14*, 24.
[5] V. Raineri, S. Coffa, E. Szilagyi, J. Gyulai, E. Rimini, *Phys. Rev. B* **2000**, *61*, 937.
[6] WebElements, http://www.webelements.com/ (accessed: September 1993).
[7] R. Livengood, S. Tan, Y. Greenzweig, J. Notte, S. McVey, *J. Vac. Sci. Technol., B* **2009**, *27*, 3244.
[8] R. Siegele, G. C. Weatherly, H. K. Haugen, D. J. Lockwood, L. M. Howe, *Appl. Phys. Lett.* **1995**, *66*, 1319.
[9] L. A. Giannuzzi, R. Geurts, J. Ringnalda, *Microsc. Microanal.* **2005**, *11*, 828.
[10] Y. C. Wang, D. G. Xie, X. H. Ning, Z. W. Shan, *Appl. Phys. Lett.* **2015**, *106*, 081905.
[11] K. E. Petersen, *Proc. IEEE* **1982**, *70*, 420.
[12] D. J. Eaglesham, A. E. White, L. C. Feldman, N. Moriya, D. C. Jacobson, *Phys. Rev. Lett.* **1993**, *70*, 1643.
[13] M. L. David, M. F. Beaufort, J. F. Barbot, *J. Appl. Phys.* **2003**, *93*, 1438.
[14] C. Griffioen, J. Evans, P. De Jong, A. Van Veen, *Nucl. Instrum. Methods Phys. Res., Sect. B* **1987**, *27*, 417.
[15] S. M. Myers, D. M. Follstaedt, *J. Appl. Phys.* **1996**, *79*, 1337.
[16] V. Raineri, M. Saggio, *Appl. Phys. Lett.* **1997**, *71*, 1673.
[17] A. V. Veen, C. Griffioen, J. Evans, presented at *MRS Proc.,* Boston, USA, January **1987**.
[18] V. Raineri, S. U. Campisano, *Appl. Phys. Lett.* **1996**, *69*, 1783.
[19] S. Estreicher, J. Weber, A. Derecskei-Kovacs, D. Marynick, *Phys. Rev. B* **1997**, *55*, 5037.
[20] V. Raineri, G. Fallica, S. Libertino, *J. Appl. Phys.* **1996**, *79*, 9012.
[21] M. Saggio, V. Raineri, R. Letor, F. Frisina, *IEEE Electron Device Lett.* **1997**, *18*, 333.
[22] T. Takagahara, K. Takeda, *Phys. Rev. B* **1992**, *46*, 15578.
[23] M. A. Okuniewski, Y. Ashkenazy, B. J. Heuser, R. S. Averback, *J. Appl. Phys.* **2004**, *96*, 4181.
[24] Z. Shan, G. Adesso, A. Cabot, M. Sherburne, S. S. Asif, O. Warren, D. Chrzan, A. Minor, A. Alivisatos, *Nat. Mater.* **2008**, *7*, 947.
[25] D. C. Joy, B. J. Griffin, *Microsc. Microanal.* **2013**, *19*, 854.
[26] J. Ziegler, J. Biersack, U. Littmark, *The Stopping and Ranges of Ions in Solids*, Pergamon, NY **1985**.
[27] R. Siegele, G. Weatherly, H. Haugen, D. Lockwood, L. Howe, *Appl. Phys. Lett.* **1995**, *66*, 1319.
[28] V. Reutov, A. Sokhatskii, *Tech. Phys. Lett.* **2002**, *28*, 615.
[29] J. F. Ziegler, M. D. Ziegler, J. P. Biersack, *Nucl. Instrum. Methods Phys. Res., Sect B* **2010**, *268*, 1818.
[30] J. Williams, J. Field, M. Swain, presented at *MRS Proc.,* Boston, USA, January **1993**.
[31] A. Witvrouw, F. Spaepen, *J. Appl. Phys.* **1993**, *74*, 7154.
[32] C. Volkert, *J. Appl. Phys.* **1993**, *74*, 7107.
[33] S. Roorda, J. M. Poate, D. Jacobson, B. Dennis, S. Dierker, W. Sinke, *Appl. Phys. Lett.* **1990**, *56*, 2097.
[34] J. Custer, M. O. Thompson, D. Jacobson, J. Poate, S. Roorda, W. Sinke, F. Spaepen, *Appl. Phys. Lett.* **1994**, *64*, 437.
[35] F. Spaepen, *Acta Metall.* **1977**, *25*, 407.
[36] A. S. Argon, M. J. Demkowicz, *Metall. Mater. Trans. A* **2008**, *39*, 1762.
[37] C. A. Volkert, *J. Appl. Phys.* **1991**, *70*, 3521.
[38] D. M. Follstaedt, J. Knapp, S. Myers, *J. Mater. Res.* **2004**, *19*, 338.

Received: May 25, 2016
Revised: July 11, 2016
Published online:

© 2016 Wiley-VCH Verlag GmbH & Co. KGaA, Weinheim

DOI: 10.1002/smll.201601753